Tailoring Structural, Chemical, and Photocatalytic Properties of ZnO@β-SiC Composites: The Effect of Annealing Temperature and Environment

Bisweswar Santra, Saptarshi Pal, Sabyasachi Saha, and Aloke Kanjilal*

Read Online

ACCESS | Metrics & More | Article Recommendations | SI Supporting Information

ABSTRACT: For achieving unified functionalities of rare-earth free materials, the development of innovative zinc oxide and β-silicon carbide (ZnO@β-SiC) composites by a solid-state reaction method is presented. The evolution of zinc silicate (Zn_2SiO_4) is evidenced by X-ray diffraction when annealed in air beyond 700 °C. Detailed X-ray photoelectron spectroscopy and Fourier transform infrared spectroscopy analyses reveal the involvement of silicon dioxide in forming Zn_2SiO_4. Transmission electron microscopy and the associated energy-dispersive X-ray spectroscopy elucidate the evolution of the zinc silicate phase at the ZnO/β-SiC interface, though it can be averted by vacuum annealing. These results manifest the importance of air in oxidizing SiC before a chemical reaction with ZnO from 700 °C. Finally, ZnO@β-SiC composites are found to be promising for methylene blue dye degradation under ultraviolet radiation, but the annealing above 700 °C is detrimental due to the evolution of a potential barrier in the presence of Zn_2SiO_4 at the ZnO/β-SiC interface.
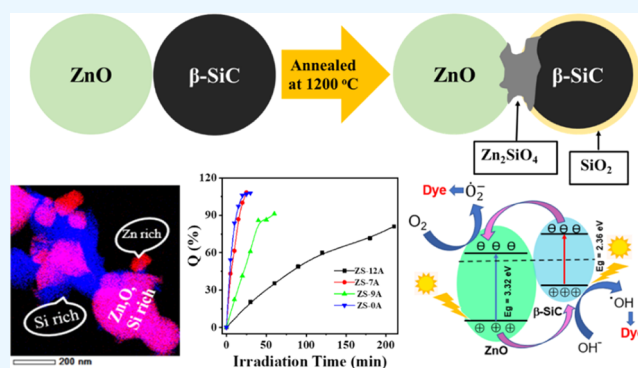
INTRODUCTION

Composite materials have made a paradigm change in materials science and engineering due to the possibility of unifying the independent properties of the technologically important constituent materials.[1,2] Although the composite materials are primarily developed from mechanical perspectives,[3,4] they have now attracted considerable interest in bringing a revolution in device applications by controlling the relevant properties like optical,[5,6] magnetic,[7,8] electrical,[9,10] etc. This requires a judicial choice of appropriate materials for specific applications and also the processing conditions for overcoming individual limitations. The composites of optically active and electronically superior radiation hard materials would be very promising in this respect for a wide range of optoelectronic applications. For instance, zinc oxide (ZnO) with a direct band gap ($E_g \sim 3.37$ eV) and large exciton binding energy (~ 60 meV) is very attractive for having high electron mobility (~ 210 cm^2 V^{-1} s^{-1}) and excellent chemical and thermal stabilities.[11,12] On the contrary, high thermal conductivity (~ 4.9 W cm^{-1} K^{-1}), high electrical breakdown field, and chemical stability make silicon carbide (SiC) a potential candidate for high-temperature, high-frequency, and high-power device applications.[13−16] The composites of these two materials would therefore be promising for large-scale optical and electrical applications[17−19] including photocatalytic activity.

Considering photocatalysis, ZnO has emerged as an efficient and promising semiconductor for its outstanding performance compared to other complementary materials like TiO$_2$, WO$_3$, SnO$_2$, CeO$_2$, etc.[23] The photocatalytic efficiency of ZnO is, however, greatly reduced by its high recombination rate of photogenerated electrons and holes and also the serious photocorrosion effect in the aqueous medium.[24] Hence, several modifications have been considered for increasing the efficiency of ZnO, such as doping with metals,[25−27] non-metals,[28,29] or rare-earth elements[30] or by making composite materials. In particular, composites of ZnO with materials, such as Al$_2$O$_3$, SiO$_2$, glass, graphene, reduced graphene oxide, carbon nanotubes, etc., have recently attracted significant attention for improving the photocatalytic activity by over-coming individual limitations.[31−35]

On the other hand, as an environment-friendly narrow-band-gap (2.3−3.3 eV for different polytypes) semiconductor with high mechanical strength, pore volume, and surface area, SiC is found to be suitable for achieving high catalytic efficiency in a wide (UV to visible) spectral range by making composites with

ZnO, TiO$_2$, BiVO$_4$, WO$_3$, SnO$_2$, etc.[20] The main advantage of SiC here is the capability to inject photogenerated electrons from its conduction band (CB) to the CB of adjacent metal oxide via the charge transfer mechanism. This process thereby suppresses the charge recombination rate and helps in degrading the organic contaminants efficiently in an aqueous medium.[20] Extensive investigation of the photocatalytic activity of ZnO@SiC composites is however limited in the literature, where the samples were mainly prepared by a chemical route.[20−22] In fact, the influence of annealing temperature on these composites and their impact on photocatalytic activities have not yet been explored to the best of our knowledge. This knowledge gap suggests that further studies are needed to understand the impact of annealing temperature on the photocatalytic properties of ZnO@SiC composites. The solid-state synthesis of composite materials in this respect is considered to be far superior to that of the chemical route in controlling the relative fraction of constituent materials in making composites. It is therefore important to not only examine the influence of the solid-state reaction in forming ZnO@SiC composites with and without annealing in air and vacuum but also explore the corresponding structure and chemical properties in controlling the photocatalytic performance in a systematic way.

In this article, we therefore focus on the development of ZnO@β-SiC composites by the solid-state reaction method and the corresponding change in structural and chemical properties with increasing annealing temperature up to 1200 °C in air. X-ray diffraction (XRD) analysis suggests the formation of the Zn$_2$SiO$_4$ phase above 700 °C, where the X-ray photoelectron spectroscopy (XPS) and Fourier transform infrared spectroscopy (FTIR) show the appearance of SiO$_2$ till 1200 °C. The evolution of zinc silicate at the ZnO/β-SiC interface has further been demonstrated by transmission electron microscopy (TEM), though this can be averted by vacuum annealing. Finally, the ZnO@β-SiC composite is shown to be beneficial for photocatalytic degradation of the methylene blue (MB) aqueous solution under exposure to ultraviolet (UV) radiation, whereas this ability gradually degrades with increasing annealing temperature and is justified in the light of the development of a potential barrier due to the formation of zinc silicate at the ZnO/β-SiC interface.

EXPERIMENTAL DETAILS

Commercially available ZnO (purity 99.99%, Sigma-Aldrich) and β-SiC (purity 99.99%, Alfa-Aeser) powders were mixed in equal weight percentages. After grinding this mixture with an automated mortar and pestle (Altis Instruments) for 2 h at 45 rpm, it was pelletized by applying 5 ton pressure using a hydraulic press for 10 min. A set of pellets was annealed at 700, 900, 1100, and 1200 °C for 90 min in a muffle furnace (MF-1400P, Metrex Instruments). Here, the unannealed ZnO@β-SiC composite is called ZS-0A, whereas the annealed ones at 700, 900, 1100, and 1200 °C in air are named ZS-7A, ZS-9A, ZS-11A, and ZS-12A, respectively, in the following.

The structural behavior of the ZnO@β-SiC composites as well as pure ZnO and β-SiC was examined by XRD (Bruker, D8-Discover) in the coupled θ−2θ mode over a 2θ range of 20−80° with Cu-Kα radiation (λ = 0.154 nm). The microstructural study was conducted by TEM using a probe-corrected Jeol (JEM ARM 200F) system operated with an accelerating voltage of 200 kV, where the elemental analysis was carried out by attached energy-dispersive X-ray spectros-

copy (EDX). The XPS measurements were also performed with Al Kα radiation (1486.6 eV) from a monochromatic source, where the photoelectrons were analyzed by a hemispherical electron analyzer fitted with a 128-channel detector in a Thermo Scientific K-Alpha+ XPS spectrometer. The sample surfaces were sputter-cleaned in situ by 1 keV Ar$^+$ ions before data acquisition. All of the spectra were collected in normal emission geometry, where the binding energy (B.E.) scale of the measured kinetic energy was calibrated from the Fermi edge (E_F) of a gold foil, while a charge neutralizer gun was employed during data acquisition. The functional groups were further monitored by FTIR in diamond attenuated−total reflection mode in a Thermo Fisher Scientific Nicolet iS5 FTIR spectrometer. The photocatalytic activities were finally examined by following the degradation of the mixture of a 4 ppm MB aqueous solution with ∼0.18 g of the ZnO@β-SiC composite under UV exposure. Before the photocatalytic decomposition experiment, the suspension of MB and the photocatalyst was magnetically stirred in the dark for 30 min to achieve adsorption/desorption equilibrium. A 125 W medium-pressure mercury lamp (spectral range of 250−400 nm) was used as a UV source, where the mixed solution was irradiated at regular intervals. After that, a 4 mL solution was collected from this mixture and centrifuged at a speed of 3000 rpm for 10 min each. The supernatant was then collected by a micropipette and analyzed by UV−visible (UV−vis) spectroscopy (Shimadzu SolidSpec-3700) to monitor the changes in the absorbance of the obtained MB solution.

RESULTS AND DISCUSSION

Figure 1 displays the XRD patterns of the ZnO@β-SiC composites before and after annealing in air up to 1200 °C.
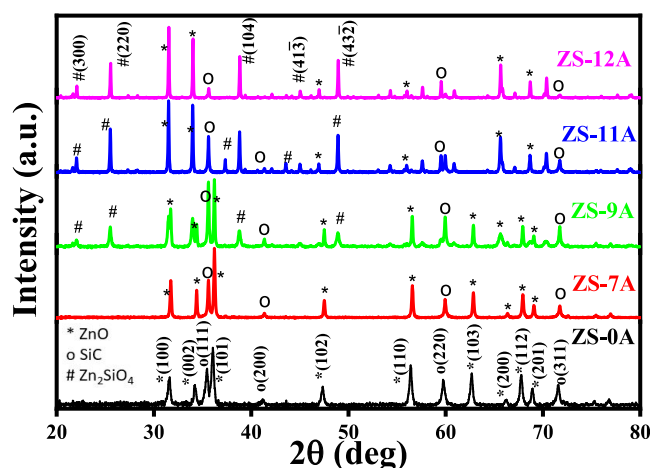
Figure 1. Typical XRD patterns of the ZnO@β-SiC composites before annealing (ZS-0A) and after annealing in air at 700 °C (ZS-7A), 900 °C (ZS-9A), 1100 °C (ZS-11A), and 1200 °C (ZS-12A). The diffraction peaks of ZnO and β-SiC are marked by "*" and "o", respectively, whereas the additional reflections from the Zn$_2$SiO$_4$ phase are marked by the "#" symbol.

The formation of the polycrystalline Zn$_2$SiO$_4$ phase is clearly visible here beside the characteristic peaks of ZnO and β-SiC (marked by "*" and "o"). In fact, the reflections at 2θ = 31.79°, 34.45°, 36.28°, 47.57°, 56.65°, 62.92°, 66.44°, 68.02°, and 69.16° and 35.63°, 41.42°, 60.03°, 71.84°, and 75.56° are from the (100), (002), (101), (102), (110), (103), (200), (112), and (201) and (111), (200), (220), (311), and (222) planes of
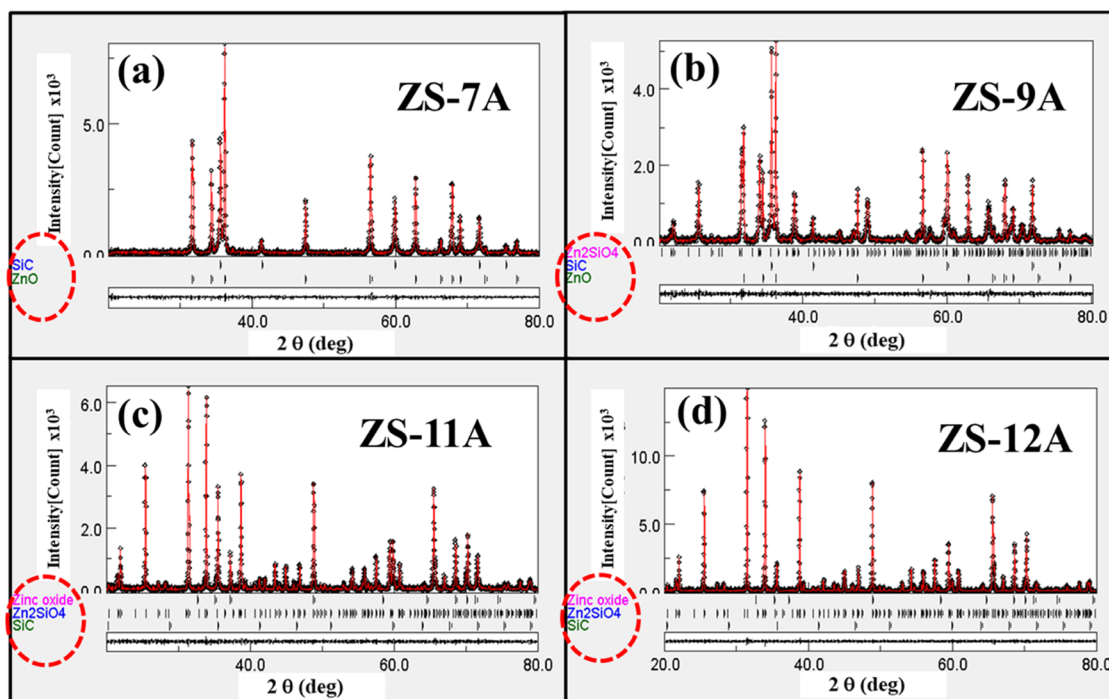
Figure 2. Rietveld refinements of the XRD patterns of ZnO@β-SiC composites after annealing in air at (a) 700 °C, (b) 900 °C, (c) 1100 °C, and (d) 1200 °C, represented as ZS-7A, ZS-9A, ZS-11A, and ZS-12A, respectively. The residual for each fitting is shown just below the respective XRD pattern. The components used for fitting each XRD pattern are highlighted by enclosing them with red dashed curves.

Table 1. Extracted Structural Parameters from the Rietveld Refinements of the ZnO@β-SiC Composites

sample(s)	components	phases	vol. fraction (%)	cell length (Å) a	cell length (Å) c	lattice strain (10^{-4})
ZS-7A	ZnO	wurtzite ($P63mc$)	42	3.25	5.21	7.69
	SiC	cubic ($F\bar{4}3m$)	58	4.36		6.25
ZS-9A	ZnO	wurtzite ($P63mc$)	40	3.25	5.20	6.53
	SiC	cubic ($F\bar{4}3m$)	50	4.36		4.01
	Zn_2SiO_4	trigonal ($R\bar{3}H$)	10	13.93	9.32	6.00
ZS-11A	ZnO	wurtzite ($P63mc$)	10	3.15	5.08	6.01
	SiC	cubic ($F\bar{4}3m$)	26	4.36		6.74
	Zn_2SiO_4	trigonal ($R\bar{3}H$)	64	13.94	9.31	4.98×10^{-3}
ZS -12A	ZnO	wurtzite ($P63mc$)	2	3.16	5.08	6.00
	SiC	cubic ($F\bar{4}3m$)	20	4.36		3.38
	Zn_2SiO_4	trigonal ($R\bar{3}H$)	78	13.95	9.32	4.45×10^{-1}

ZnO and β-SiC in ZS-0A and ZS-7A, respectively, while the additional peaks at 2θ = 22.12°, 25.59°, 38.90°, and 49.02° are found to be originated from the (300), (220), (104), and (33$\bar{3}$) planes of Zn_2SiO_4 from 900 °C onward (marked by "#" symbol). Here, θ is the Bragg angle. The XRD patterns of the reference samples (i.e., ZnO and β-SiC) are also exhibited in Figures S1 and S2, respectively, for clarity. All of the reflected peaks are indexed according to the JCPDS files for ZnO (# 01-079-0207) and β-SiC (# 00-029-1129).

To confirm the Zn_2SiO_4 phase formation at 900 °C and above, the XRD patterns have further been analyzed carefully by Rietveld's refinement with MAUD software. The fitting results (in red) are superimposed on the respective experimental patterns (in black) in Figure 2a−d for direct comparison. The components required for the fitting process are encircled by red dashed curves, and the extracted parameters like volume fraction, strain, and cell parameters are summarized in Table 1. As expected, only the reflections from ZnO and β-SiC are obtained in ZS-7A, whereas α-Zn_2SiO_4 with an $R\bar{3}H$ space group symmetry is unveiled in ZS-9A, ZS-11A, and ZS-12A, in good agreement with the results of Valiveti et al.[36] Moreover, Rivera−Enriquez et al.,[37] however, reported the formation of amorphous β-zinc silicate in coprecipitated samples at 650 °C, but it was found to be transformed to the α-phase at 900 °C. On the other side, Wahab et al.[38] demonstrated a transformation of β zinc silicate to the α-phase when annealed the mixture of ZnO and WRHA (96% SiO_2) at ~950 °C.

For understanding the effect of the surrounding atmosphere in zinc silicate phase formation (see Figure 1), another ZnO@β-SiC composite sample was prepared by annealing in vacuum (working pressure of ~2 × 10^{-6} mbar) at 900 °C. The phase determination was carried out by XRD, though no secondary phase was found here (see Figure S3 in the Supporting Information). The above results are therefore implying that the

surrounding air plays an important role in forming the secondary phase during annealing.

To explore the underlying mechanism behind the Zn_2SiO_4 phase formation, the samples have further been characterized by XPS. Since ZS-12A has given the maximum volume fraction in Rietveld analysis (see Table 1), this particular sample has been considered here for detailed chemical analysis. The survey scan of ZS-12A in Figure 3 indicates the presence of
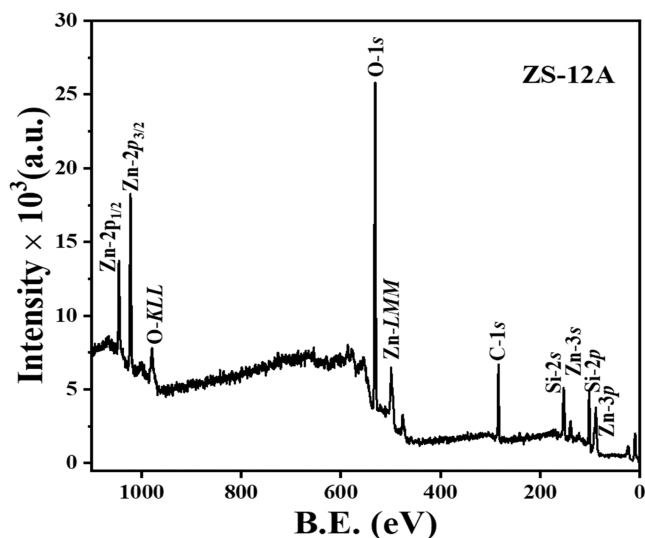
Figure 3. Typical survey scan of ZS-12A during XPS measurement showing the core levels of Zn, Si, C, and O along with Zn-LMM and O-KLL Auger peaks, where 0 eV represents the Fermi level.

only Zn, O, Si, and C, while the high-resolution XPS of the C 1s, O 1s, Si 2p, and Zn 2p levels is presented in Figure 4a–d, respectively. Close inspection of the C 1s, O 1s, and Si 2p peaks, however, reveals an asymmetric nature, suggesting the presence of multiple chemical states, which have been identified by deconvoluting them with the Voigt (70% Gaussian and 30% Lorentzian) function after Shirley background subtraction using standard CasaXPS processing software.

The C 1s peak in Figure 4a has been deconvoluted by three components: (i) C–C (284.5 eV), (ii) C–Si (283.5 eV), and (iii) C–O (285.52 eV). Here, the C–C and C–Si bonds can be attributed to the segregated carbon and the carbon in β-SiC residing on the sample surface, respectively,[73] whereas the signal of C–O at ~285.62 eV is ascribed to be originated from the reaction of C in β-SiC with the surrounding O during high-temperature annealing.[38−42] Similarly, the O 1s peak has been deconvoluted into three components (see Figure 4b), where the peaks are found to be centered at ~530.61 eV (red), 531.58 eV (violet), and 532.48 eV (orange). The peak situated at ~530.61 eV can be assigned to the lattice oxygen of ZnO ($O^{2−}$),[43,44,50,51] while the peak at ~531.58 eV is most likely associated with the formation of a new phase. In fact, this is corroborated by an additional component revealed in Si 2p peak fitting (see Figure 4c) related to the Si–O–Zn bond.[45,46] Looking at the XRD results in Figure 2, it appears that this new component in the above XPS results seems to be related to the zinc silicate phase.[45,46] Now the third component peaking at ~532.48 eV for O 1s level reflects the existence of the Si–O–Si bond.[47] Interestingly, the deconvolution of Si 2p in Figure 4c gives a component at ~103.31 eV signifying the existence of

SiO_2.[48,49] The existence of SiO_2 is found to be important for understanding the dynamics behind the formation of the zinc silicate phase in the ZnO@β-SiC composites during high-temperature annealing in air, and it will be discussed in the following. Again, the peaks originating at ~101.18 and 102.38 eV in Si 2p are found to be associated with β-SiC[50] and zinc silicate[51] phases, respectively. Moreover, a doublet of Zn $2p_{3/2}$ (1021.96 eV) and Zn $2p_{1/2}$ (1045.12 eV) for the Zn 2p level is clearly visible in Figure 4d, giving an area ratio of ~2 and a peak separation of ~23 eV. For comparing these results, the chemical composition of ZnO and β-SiC has also been analyzed as documented in Figure S4. The extracted peak positions and full width at half-maximum (FWHM) for all of the components are also summarized in Table S1 for clarity. Although no significant change is found in the Zn $2p_{3/2}$ and Zn $2p_{1/2}$ peak positions in Z-12A and ZS-12A, a clear increase in FWHM is, however, evident for the latter sample (see Table S1 in the Supporting Information) due to the modification in the local chemical environment of the Zn atom.

The microstructural origin of the Zn_2SiO_4 phase with increasing temperature has further been investigated by TEM. Typical bright-field (BF) TEM images of ZS-7A, ZS-9A, and ZS-12A are displayed in Figure 5a–c, respectively. As discerned from the corresponding insets, the average grain size in ZS-7A is measured to be 80−100 nm, whereas it enhances gradually to 500 nm or above in ZS-12A due to Ostwald ripening.[52] Selected area electron diffraction (SAED) patterns of the respective samples have also been monitored to follow the temperature-dependent structural modification, as exhibited in Figure 5d−f. Close inspection suggests that the clusters in any case are polycrystalline in nature, though the intense and bright spots in Figure 5d indicate the formation of bigger crystallites.

Given the evolution of the secondary phase in Figure 1, the appearance of some incomplete concentric rings with many small bright spots in Figure 5e is most likely associated with the lowering of the crystallinity of the constituent materials in ZS-9A due to chemical reaction at the ZnO/β-SiC interfaces. However, the relatively discrete streaky features in Figure 5f reveal the existence of strain in this newly formed secondary phase by suppressing the contribution of the primary materials. In order to explore this phenomenon, high-resolution TEM (HRTEM) analysis has further been conducted on ZS-12A. A typical BF-TEM image of ZS-12A is displayed in Figure 6a, showing a clear contrast difference in some regions highlighted by orange and white dashed circles, as well as by a yellow rectangular box.

Since the mass of Zn_2SiO_4 (222.84 g/mol) is much more than those of ZnO (81.38 g/mol) and SiC (40.10 g/mol), a contrast difference is expected in such a mixed medium.[53] It is therefore expected to have a zinc silicate phase in dark regions. The surrounding mild/light gray region may have ZnO and/or SiC including SiO_2 (60.08 g/mol) due to small variation in their molar masses, where the latter was revealed by XPS analysis (see Figure 4). This makes it difficult to identify different components in Figure 6a. Close inspection of the yellow box area further shows a wavy behavior, which often appears due to strain.

For a better understanding, the HRTEM image of this area has also been recorded as the one shown in Figure 6b. As can be seen, the lattice fringes are visible, though they are prominent in Figure 6c when the yellow box region in Figure 6b is further magnified. The interplanar spacing (d) has been
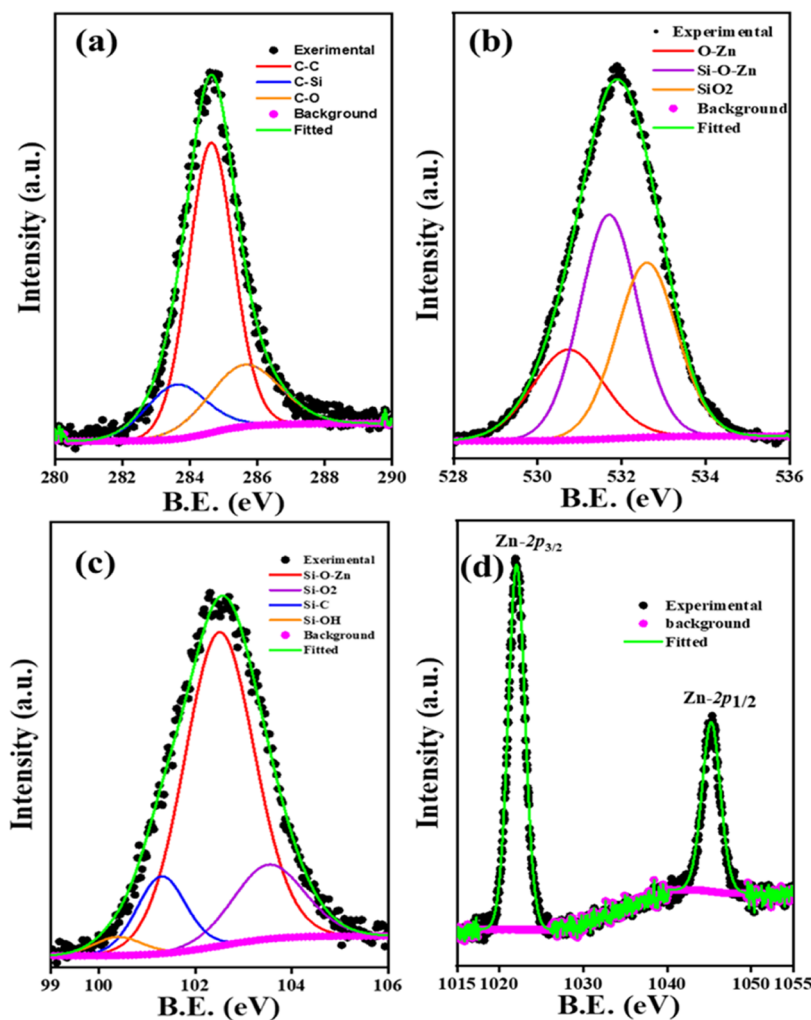
Figure 4. High-resolution XPS results of ZS-12A at (a) C 1s, (b) O 1s, (c) Si 2p, and (d) Zn 2p levels (dark-filled circles) deconvoluted by the Voigt function (solid lines) after Shirley background subtraction (purple-filled circles). The fitted results are shown by green lines.
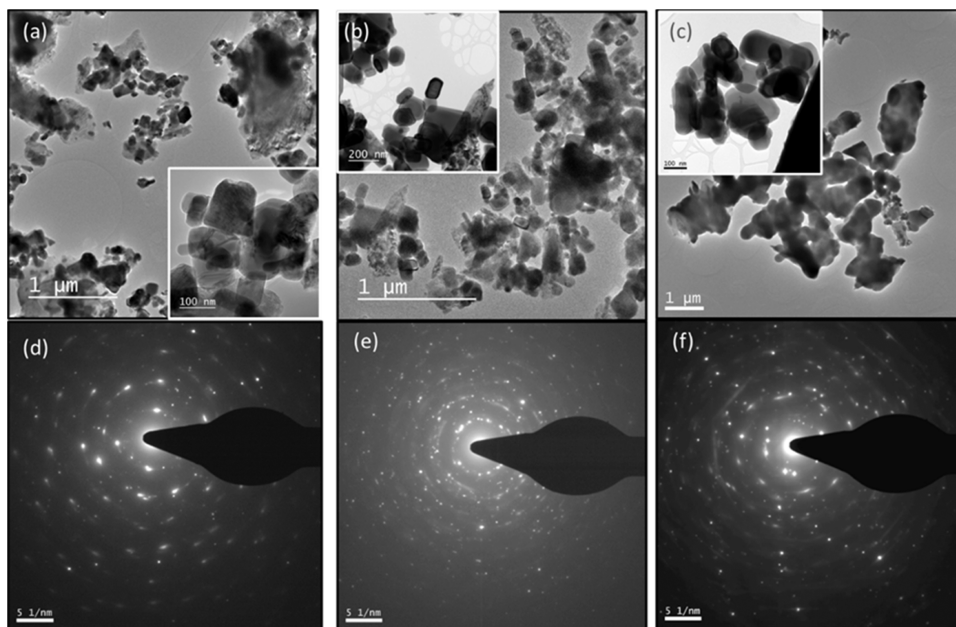
Figure 5. (a−c) Typical BF-TEM images of the ZnO@β-SiC composites after annealing at 700 °C (a), 900 °C (b), and 1200 °C (c) in air, where the magnified images are shown in the respective insets. The corresponding SAED patterns are also shown in (d−f).
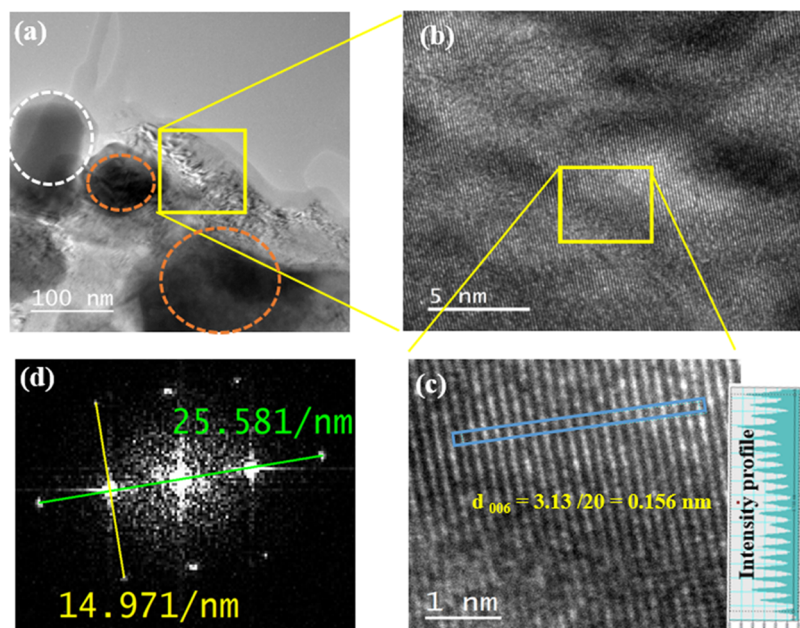
Figure 6. (a) BF-TEM image of ZS-12A, where the regions with prominent gray and dark contrasts are marked by the close white and red dashed curves. The light gray region is highlighted by a yellow square showing the existence of fringe-like features from strain, where the HRTEM image of this region is shown in (b). Moreover, the region highlighted by a yellow square in (b) is further magnified in (c), showing the atomic planes. The intensity profile along the trace within a blue rectangular area is also presented for clarity. (d) The FFT of the recorded HRTEM image in (c) along the [100] zone axis.
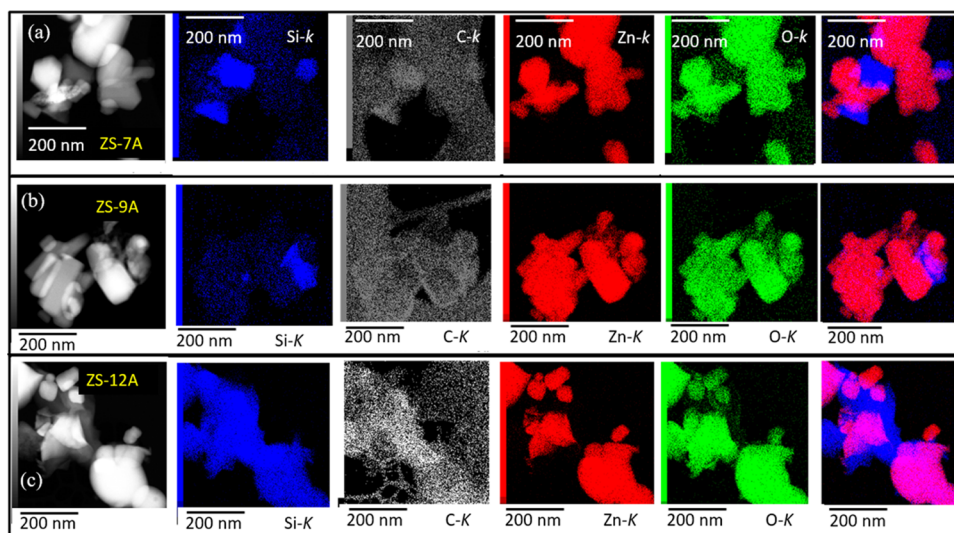
Figure 7. HAADF images of the ZnO@β-SiC composites after annealing at 700 °C (a), 900 °C (b), and 1200 °C (c) in air, where the EDX mappings of the respective samples at the K edge of Si (blue), C (gray), Zn (red), and O (green) are exhibited in the top, middle, and bottom panels. The extreme right-side figure for each temperature represents the EDX mapping after overlapping all data of the constituent elements.

estimated from a trace across 20 planes (illustrated by the adjacent intensity profile for the blue rectangular box) in Figure 6c, giving an average value of 0.156 nm. This corresponds to the (006) plane of the Zn_2SiO_4 phase [JCPDS file # 01-083-2270]. Fast Fourier transform (FFT) of Figure 6c is displayed in Figure 6d along the [100] zone axis. The d spacing has also been extracted from the diffraction spots in FFT to be $d_{006} = 1/(25.58/4) = 0.156$ nm and $d_{090} = 1/(14.97/2) = 0.134$ nm, confirming the formation of the Zn_2SiO_4 phase. It is therefore clear that the wavy feature as well as the mild/light gray contrast beyond the darkest region in Figure 6a can be attributed to the adjacent thinner region of

the Zn_2SiO_4 crystallites. The EDX mapping was further conducted for exploring the elemental distribution.

The Z contrast intensity of the samples was also investigated by high-angle annular dark-field (HAADF) imaging as the contrast depends on the weighted sum of $Z^{1.7}$.[54] The HAADF images of ZS-7A, ZS-9A, and ZS-12A are shown at the extreme left of Figure 7a−c, respectively. Here, the white region signifies the highest Z value. For precise and accurate determination of the elemental distribution in these samples, the EDX mappings at the K edges of Si, C, Zn, and O were conducted. The results of ZS-7A, ZS-9A, and ZS-12A are documented in the upper, middle, and lower panels beside the

corresponding HAADF images (see Figure 7a−c). The overlapped EDX maps for each sample are exhibited at the extreme right of the panels in Figure 7. One can see that there are regions of overlap where both Zn and Si are present (violet), though these regions are found to be increasing with annealing temperature. Looking at the XRD results (see Figures 1 and 2) and the microstructural information (Figure 6), Figure 7 therefore confirms the evolution of the Zn_2SiO_4 phase from the ZnO/β-SiC interfaces at the expense of constituents ZnO and β-SiC.

Since the existence of SiO_2 is found in ZS-12A by XPS (see Figure 4), FTIR measurement has also been carried out to validate this observation.[55] In fact, the systematic FTIR studies of the presently investigating samples give the platform to follow the involvement of the surrounding (air and vacuum) environment in forming the Zn_2SiO_4 phase at the ZnO/SiC interfaces during annealing.

The FTIR spectroscopy results for both the as-prepared and air-annealed ZnO@β-SiC composites in the transmittance mode in the range of 400−4000 cm^{-1} are exhibited in Figure 8.
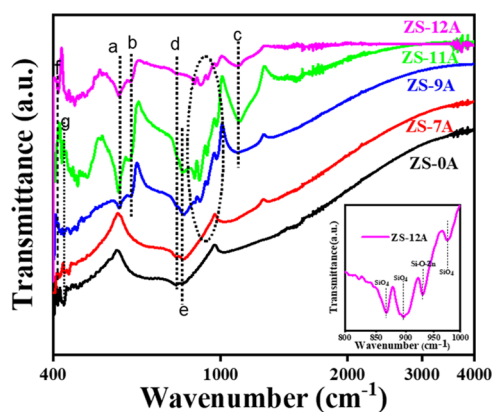

Figure 8. Typical transmission FTIR spectra of ZnO@β-SiC composites before annealing (ZS-0A) and after annealing at 700 °C (ZS-7A), 900 °C (ZS-9A), 1100 °C (ZS-11A), and 1200 °C (ZS-12A) in air. Different modes are identified, and they are marked by vertical dashed lines. The peaks related to zinc silicate are marked by a close dashed curve, which is further magnified in the inset for clear findings of SiO_4 and Si−O−Zn modes.

As discerned, the appearance of peaks at ∼870 cm^{-1} (SiO_4), 900 cm^{-1} (SiO_4), 931 cm^{-1} (Si−O−Zn), and 980 cm^{-1} (SiO_4) signifies the formation of the zinc silicate phase[56] in ZS-12A. Since these peaks are relatively weak in ZS-12A (encircled by a dashed loop), this is projected again in the range of 800−1000 cm^{-1} for clarity (see inset). In fact, the peak at 931 cm^{-1} is the characteristic peak of Zn_2SiO_4.[56] The peaks marked by dashed lines "*a*" and "*b*" located at ∼573 and ∼611 cm^{-1}, respectively, can be assigned to the asymmetric stretching modes of ZnO_4 in the Zn_2SiO_4 crystal,[57,58] while the peak at ∼1097 cm^{-1} (indicated by dashed line "*c*") can be attributed to the Si−O−Si stretching mode.[59−61] Moreover, a peak at ∼567 cm^{-1} was previously reported as the characteristic absorption peak of the Zn−O stretching mode.[28,29] Looking at Figure 8, it is therefore clear that the peak at ∼567 cm^{-1} up to 700 °C arises from the vibrational mode of ZnO_4,[57] whereas it is drastically suppressed in the presence of crystalline Zn_2SiO_4[57,58] from ZS-9A. However, the presence of two other transmittance peaks indicated by dashed lines "*d*" and "*e*" at ∼778 and 816 cm^{-1} can be assigned to the TO and LO modes of SiC,

respectively.[62] These peaks are, however, negligible in ZS-12A in the presence of strong zinc silicate peak formation, indicating a drastic chemical reaction at 1200 °C in air. In addition, the existence of ZnO has further been confirmed in the presence of additional peaks originating at ∼407.5 and 420.8 cm^{-1} marked by dashed lines "*f*" and "*g*", respectively, by comparing the results obtained from pure ZnO (shown in Figure S5 in the Supporting Information).

To follow the origin of the Si−O−Si asymmetric stretching mode in the ZnO@β-SiC composites (see Figure 8), pure β-SiC (S-0A) and the annealed ones at 700, 900, 1100, and 1200 °C in air, called S-7A, S-9A, S-11A, and S-12A, respectively, were further examined by FTIR spectroscopy (shown in Figure 9) for direct comparison. The evolution of the silanone group
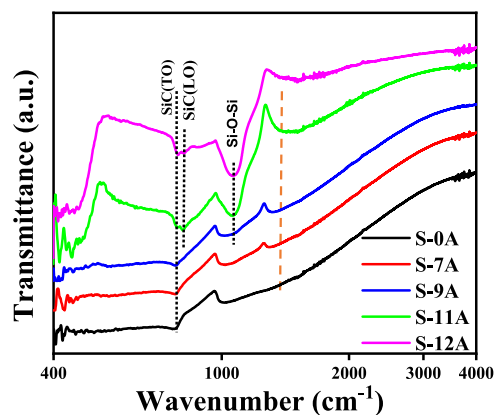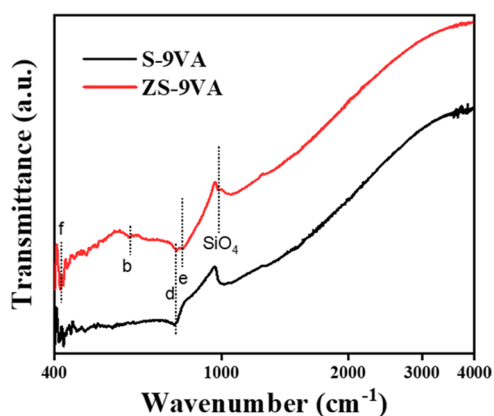

Figure 9. FTIR spectra of SiC before annealing (S-0A) and after annealing at 700 °C (S-7A), 900 °C (S-9A), 1100 °C (S-11A), and 1200 °C (S-12A) in air. The SiC(LO), SiC(TO), and Si−O−Si asymmetric stretching modes are presented by vertical dashed lines. The evolution of the silanone group at the SiC/SiO_2 interface is presented by a vertical red dashed line.

(pointed by a vertical red dashed line) at the SiC/SiO_2 interface with a weak feature (∼1305 cm^{-1})[63] from S-7A is clearly visible besides the observation of the TO (∼780 cm^{-1}) and LO (∼820 cm^{-1}) modes of SiC.[62] The key finding is that a peak at ∼1097 cm^{-1} is found to be more prominent from 900 °C, which is assigned to be related to the formation of SiO_2 in SiC.[64−67] To justify the involvement of the surrounding environment in surface oxidation, both β-SiC and the ZnO@β-SiC composite were also annealed in vacuum at 900 °C for 90 min in a horizontal split furnace (base pressure ∼2 × 10^{-6} mbar) with a heating/cooling rate of 4 °C/min, called S-9VA and ZS-9VA, respectively. The vacuum-annealed FTIR results are shown in Figure 10, demonstrating the absence of SiO_2 (∼1097 cm^{-1}) in both β-SiC and ZnO@β-SiC composite. Considering the air annealing results in Figure 9, it is clear that SiO_2 cannot be formed in β-SiC without air, in good agreement with the results of Tachiki et al.[64] Given the findings of Figures 9 and 10, the emergence of the zinc silicate phase in Figure 8 can only be explained by the production of SiO_2 via oxidizing β-SiC in air from 900 °C and the subsequent chemical reaction at the ZnO/β-SiC interface.

Here, SiO_2 is expected to be formed in β-SiC according to eq 1 by considering the involvement of oxygen from air,[66,68] which is not possible in vacuum.

$$2\ SiC(s) + 3\ O_2(g) = 2 SiO_2(s) + 2 CO(g) \qquad (1)$$
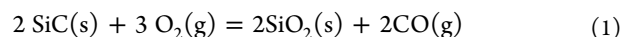
Figure 10. FTIR spectra of SiC (black) and the ZnO@β-SiC composite (red) after annealing at 900 °C in vacuum and referred to as S-9VA and ZS-9VA, respectively. Different vibrational modes of ZnO and SiC including SiO$_4$ by vertical dashed lines for a guide to the eyes.

Here, the formation of the Zn$_2$SiO$_4$ phase can be explained by the following reaction.

$$SiO_2(s) + 2\,ZnO(s) = Zn_2SiO_4(s) \tag{2}$$
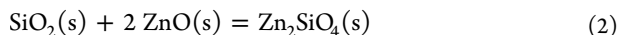
Now considering eqs 1 and 2, the formation of the Zn$_2$SiO$_4$ phase at the ZnO/SiC interfaces based on the above experimental results can be expressed as follows.

$$3\,ZnO(s) + SiO_2(s) + SiC(s)$$
$$= Zn_2SiO_4(s) + ZnO(s) + SiC(s) \tag{3}$$
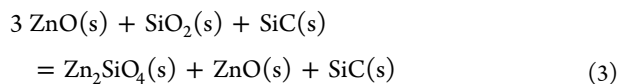
It is important to note here that the presence of excess SiO$_2$ in the XPS and FTIR analyses can be elucidated as an unreacted product, and this is expected when all of the ZnO and β-SiC grains cannot come in contact for a chemical reaction. However, SiO$_2$ seems to be in an amorphous phase, as it did not reflect in the XRD patterns (see Figure 1).

Typical absorption spectra of MB in the range of 400−800 nm for ZS-0A, ZS-7A, ZS-9A, and ZS-12A are shown in Figure S6 for different UV exposure times. The systematic reduction of absorbance signifies the gradual decrease of MB concentration by degrading the dye with the ZnO@β-SiC photocatalyst. As discerned, the complete removal of dye from the MB solution happens in a very short time for ZS-0A. It takes only 25 min to degrade completely, and to the best of our knowledge, it is the least number among all the reported time durations. However, the degradation time was found to be enhanced with the increase of annealing temperature. Figure 11a,b represents the variation of C_t/C_0 with respect to the UV exposure time, where C_0 and C_t denote the primary concentration of MB solution and the concentration after exposure to UV radiation for time t, respectively. The values of the rate constant k are calculated from the slope of the $\ln(C_0/C_t)$ versus irradiation time (t) plot using the pseudo-first-order kinetic equation, as shown in Figure 11b, showing a decrease in degradation rate with increasing annealing temperature of the ZnO@β-SiC composites.

Details of the rate constants are summarized in Table S2. As can be seen that different degradation rates are exhibited for different samples. For instance, the degradation rate for ZS-0A has only one component, whereas there are three, K_1, K_2, and K_3, for the highest processing one (ZS-12A).
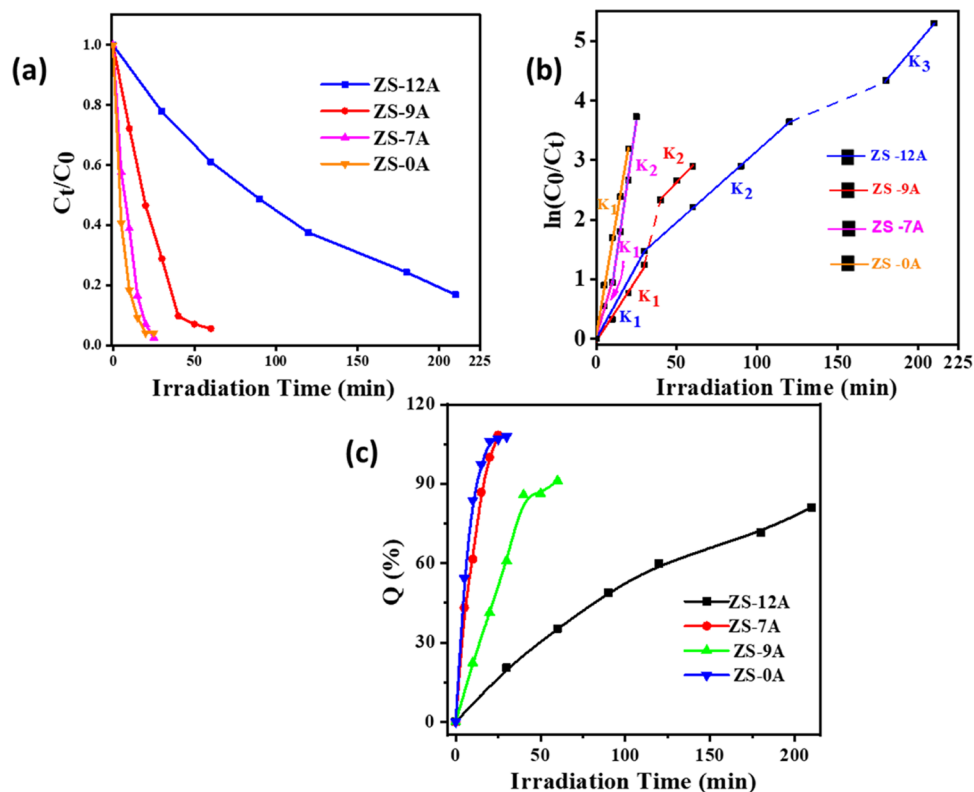
Figure 11. (a) Photocatalytic degradation of MB under UV light illumination of ZS-0A, ZS-7A, ZS-9A, and ZS-12A.(b) The corresponding pseudo-first-order kinetic fit for MB photodegradation under UV light. (c) The change in photocatalytic dye degradation efficiency (Q) with increasing white light exposure time for MB.
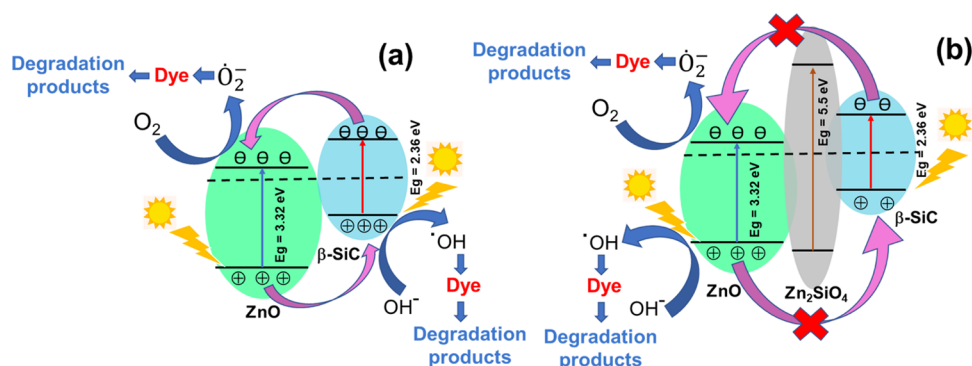
Figure 12. Schematic representation of the charge transfer mechanism across the ZnO/β-SiC interface during the MB dye degradation process without (a) and with (b) the formation of the interfacial Zn_2SiO_4 phase.

The observed change in rate constants with increasing annealing temperature can be explained in the light of Zn_2SiO_4 phase formation. It may be noted that the maximum absorption peak shows a blue shift (see Figure S6) in nature due to the changes in the molecular geometry of MB during the reaction with the photocatalyst.[72]

The photocatalytic dye degradation efficiency (Q) has further been calculated by the formula $Q = (A_0 - A_t)/A_0 \times 100\%$, where A_0 and A_t are the absorbances of the MB solution before and after exposure for t min to UV irradiation, respectively. The extracted Q values are projected in Figure 11c. For the ZS-0A and ZS-7A samples, the maximum dye degradation efficiency was found to reach 100% in 25 min, while for those samples annealed at higher temperatures, the efficiency diminishes gradually. For instance, an efficiency value of 80% was attained in 3 h for ZS-12A.

According to the existing literature, the composites of ZnO and SiC often form a porous and less ordered structure at low annealing temperatures, where amorphous SiC may also be present in this stage. However, the crystallinity and grain size of both ZnO and β-SiC have been shown to be increased with the increase in annealing temperature, and in turn, it improves their chemical and structural stability and the subsequent enhancement of photocatalytic activity.[75−78] On the contrary, the crystal structure of ZnO has also been shown to aggregate and form bigger clusters in the β-SiC matrix at high temperatures, and as a result, this negatively affects the photocatalytic activity due to the lower surface-to-volume ratio.[36,74] However, none of these models can be used to explain the present findings due to the presence of the Zn_2SiO_4 phase at the ZnO/β-SiC interface during thermal annealing. Under these circumstances, the present intriguing MB dye degradation phenomenon (Figure 11) can be explained in light of the gradual development of the Zn_2SiO_4 phase at the ZnO/β-SiC interface and its subsequent effect on the charge separation and its transport capability, as shown in Figure 12.

For the as-prepared sample as well as the sample prepared by annealing at 700 °C in air, a fast photocatalytic degradation effect has been revealed and this phenomenon can be explained by considering the direct formation of the ZnO/β-SiC heterojunction in the ideal ZnO@β-SiC composite (see Figure 12a), which therefore makes it easy to transport photogenerated charge carriers across the interface due to the band alignment. In fact, during UV irradiation, both ZnO and β-SiC in the as-prepared composite (ZS-0A) are excited simultaneously and generate photoelectrons and holes at the CB and valance band (VB), respectively. Since the CB of ZnO

is lying below the CB of β-SiC, the photoexcited electrons in β-SiC are expected to be transferred to ZnO.[69,70] Moreover, the holes are transferred from ZnO to β-SiC due to the relative change in the VB position (shown schematically in Figure 12a). It is worthwhile to note that due to the indirect-band-gap nature of β-SiC, it is likely to help the electron transfer process from the CB of β-SiC to ZnO instead of nonradiative recombination within itself. These photoelectrons in ZnO then interact with the oxygen molecules present in the dye and produce free $\dot{O}_2^-$ radicals and finally degrade the MB molecules. On the other hand, photogenerated holes interact with H_2O molecules and produce hydroxyl ($^{\bullet}OH$) radicals. These strong oxidant radicals oxidize MB molecules and degrade efficiently.

However, the above charge transfer process is not straightforward in the presence of an additional Zn_2SiO_4 phase as can be seen from Figure 11. The presence of multiple rate constants with increasing annealing temperature can be explained on the ground of the gradual evolution of the Zn_2SiO_4 phase at the ZnO/β-SiC heterojunction with increasing annealing temperature (see Figure 7). This additional Zn_2SiO_4 phase with a larger band gap ($E_g = 5.5$ eV[71]) is therefore expected to create a high potential barrier at the ZnO/β-SiC interface. This is schematically illustrated in Figure 12b, while the different rate constants can be attributed to the involvement of defects with increasing annealing temperature. Given the structure (Figures 1 and 2) and microstructure (Figure 7), we believe that the rate constant K_1 is associated with the ideal formation ZnO@β-SiC composites, whereas K_2 and K_3 can be assigned to the involvement of Zn_2SiO_4 and the associated defects, respectively.

■ CONCLUSION

In summary, the development of ZnO@β-SiC composites by a solid-state reaction method and their structural stability during annealing with elevated temperatures are reported. The XRD analysis revealed the formation of the zinc silicate (Zn_2SiO_4) phase with the increase in annealing temperature in air up to 1200 °C. The Rietveld refinements did also confirm the formation of this additional phase with trigonal ($R\bar{3}H$) symmetry above 700 °C. The chemical analysis by XPS further validates the development of SiO_2 along with the formation of a secondary phase, while the FTIR results suggest the formation of amorphous SiO_2 above 700 °C. Given the XRD results, detailed TEM analysis along with EDX mapping, however, demonstrate the origin of crystalline Zn_2SiO_4 at the ZnO/β-SiC interface. Interestingly, the Zn_2SiO_4 phase was found to be avoided when the ZnO@β-SiC composites were

annealed in vacuum at 900 °C. A possible kinetics at the ZnO/β-SiC interface was proposed in the presence of atmospheric oxygen, where a newly formed SiO_2 at the surface of a crystalline β-SiC grain was found to dictate the chemical reaction with the nearby ZnO. Moreover, the photocatalytic properties of the ZnO@β-SiC composites were studied by exposing the MB aqueous phase to UV radiation, where maximum dye removal efficiency was found to be ~100% in ~25 min for ZS-0A. However, the removal rate was diminished gradually with increasing annealing temperature. This was explained here in light of the development of a high potential barrier due to the formation of Zn_2SiO_4 at the ZnO/β-SiC interface above 700 °C.

ASSOCIATED CONTENT

Data Availability Statement

The data that support the findings of this study are available within the article and from the corresponding author upon reasonable request.

(SI) Supporting Information

The Supporting Information is available free of charge at https://pubs.acs.org/doi/10.1021/acsomega.3c03957.

> XRD patterns of ZnO before and after annealing in air (Figure S1); corresponding results of β-SiC (Figure S2); XRD patterns of vacuum-annealed ZnO, β-SiC, and the ZnO@β-SiC composite are superimposed (Figure S3); HR-XPS results of the annealed ZnO and β-SiC at 1200 °C (Figure S4), details of the fitting components (Table S1); FTIR spectra of ZnO after annealing in both air and vacuum (Figure S5); typical absorption spectra of MB in the visible range for ZS-0A, ZS-7A, ZS-9A, and ZS-12A under UV irradiation for different times (Figure S6); and degradation rate constants of the unannealed and annealed ZnO@β-SiC composites (Table S2) (PDF)

AUTHOR INFORMATION

Corresponding Author

Aloke Kanjilal − *Department of Physics, School of Natural Sciences, Shiv Nadar Institution of Eminence, Gautam Buddha Nagar 201314 Uttar Pradesh, India;* ⊙ orcid.org/0000-0002-0805-4527; Email: aloke.kanjilal@snu.edu.in

Authors

Bisweswar Santra − *Department of Physics, School of Natural Sciences, Shiv Nadar Institution of Eminence, Gautam Buddha Nagar 201314 Uttar Pradesh, India*

Saptarshi Pal − *Department of Physics, Institute of Applied Sciences and Humanities, GLA University, Mathura 281406 Uttar Pradesh, India*

Sabyasachi Saha − *CEMES-CNRS and Université de Toulouse, 31055 Toulouse, France*

Complete contact information is available at:
https://pubs.acs.org/10.1021/acsomega.3c03957

Author Contributions

B.S. contributed to performing experiments and analysis, writing the original manuscript, and visualization; S.P. contributed to partial analysis, writing, and editing; S.S. performed microstructural studies; and A.K. contributed to conceptualizing the problem, validating results and analysis, and editing.

Notes

The authors declare no competing financial interest.

ACKNOWLEDGMENTS

REFERENCES

(1) Thostenson, E. T.; Li, C.; Chou, T. W. Nanocomposites in context. *Compos. Sci. Technol.* **2005**, *65*, 491−516.

(2) Islam, A.; Sharma, V. K.; Mausam, K. An analytical study of nano carbon materials for developing metal matrix nano composites. *Mater. Today: Proc.* **2021**, *45*, 2867−2870.

(3) Kumar, A.; Sharma, K.; Dixit, A. R. A review on the mechanical properties of polymer composites reinforced by carbon nanotubes and graphene. *Carbon Lett.* **2021**, *31*, 149−165.

(4) Landel, R. F.; Lawrence, E. N. *Mechanical Properties of Polymers and Composites*; CRC press, 1993.

(5) Gehr, R. J.; Boyd, R. W. Optical properties of nanostructured optical materials. *Chem. Mater.* **1996**, *8*, 1807−1819.

(6) Aziz, S. B.; Brza, M. A.; Nofal, M. M.; Abdulwahid, R. T.; Hussen, S. A.; Hussein, A. M.; Karim, W. O. A comprehensive review on optical properties of polymer electrolytes and composites. *Materials* **2020**, *13*, 3675.

(7) Saxena, A.; Godara, S. S. Magnetic Nano Composite Materials: A Review. In *AIP Conference Proceedings*; AIP Publishing LLC, 2019 030022 DOI: 10.1063/1.5123944.

(8) Grujić, A.; Talijan, N. M.; Stojanović, D.; Stajić-Trošić, J.; Burzić, Z.; Balanović, L.; Aleksić, R. Mechanical and magnetic properties of composite materials with polymer matrix. *J. Min. Metall., B* **2010**, *46*, 25−32.

(9) Sengupta, R.; Bhattacharya, M.; Bandyopadhyay, S.; Bhowmick, A. K. A review on the mechanical and electrical properties of graphite and modified graphite reinforced polymer composites. *Prog. Polym. Sci.* **2011**, *36*, 638−670.

(10) Yang, S. H.; Nguyen, T. P.; Le Rendu, P.; Hsu, C. S. Optical and electrical properties of PPV/SiO_2 and PPV/TiO_2 composite materials. *Composites, Part A* **2005**, *36*, 509−513.

(11) Özgür, Ü.; Alivov, Y. I.; Liu, C.; Teke, A.; Reshchikov, M.; Doğan, S.; Avrutin, V. C.; Cho, S. J.; Morkoç, A. H. A comprehensive review of ZnO materials and devices. *J. Appl. Phys.* **2005**, *98*, 11.

(12) Bhardwaj, S.; Gupta, A.; Kumar, G.; Sharma, P.; Kant, R.; Pandey, O. P.; Sharma, K. Comparative structural and optical studies of Al-/Sn-doped ZnO-textured films for optoelectronic application. *J. Mater. Sci.: Mater. Electron.* **2022**, *33*, 13757−13770.

(13) Adappa, R.; Suryanarayana, K.; Hatwar, H. S.; Rao, M. R. *Review of SiC Based Power Semiconductor Devices and Their Applications, 2nd International Conference on Intelligent Computing, Instrumentation and Control Technol.*; IEEE, 2019; pp 1197−1202 DOI: 10.1109/ICICICT46008.2019.8993255.

(14) Thakur, S. S.; Pradhan, S. K.; Sehgal, S.; Saxena, K. K. Experimental investigations on silicon carbide mixed electric discharge machining. *Silicon* **2023**, *15*, 583.

(15) Umezawa, H.; Nagase, M.; Kato, Y.; Shikata, S. I. High temperature application of diamond power device. *Diamond Relat. Mater.* **2012**, *24*, 201−205.

(16) Alves, L. F.; Gomes, R. C.; Lefranc, P.; Pegado, R. D.; Jeannin, P. O.; Luciano, B. A.; Rocha, F. V. *SIC Power Devices in Power Electronics: An Overview*, Brazilian Power Electronics Conf; IEEE, 2017; pp 1−8 DOI: 10.1109/COBEP.2017.8257396.

(17) Zhu, H.; Yang, H.; Du, K.; Fu, W.; Chang, L.; Pang, X.; Zeng, Y.; Zou, G. Preparation of SiC and SiC/ZnO nanocomposites and its properties. *Mater. Lett.* **2007**, *61*, 4242−4245.

(18) Platonov, V. B.; Rumyantseva, M. N.; Frolov, A. S.; Yapryntsev, A. D.; Gaskov, A. M. High-temperature resistive gas sensors based on ZnO/SiC nanocomposites. *Beilstein J. Nanotechnol.* **2019**, *10*, 1537−1547.

(19) Hwang, H.; Choi, H.; Jung, M. Dip-coating of SiO₂ onto ZnO-SiC composite membrane. *J. Energy Power Eng.* **2015**, *9*, 562−565.

(20) Qin, X.; Wang, F. Preparation and photocatalytic properties of ZnO/SiC composites for methylene blue degradation. *Appl. Phys. A* **2022**, *128*, 273.

(21) Meenakshi, G.; Sivasamy, A. Nanorod ZnO/SiC nanocomposite: An efficient catalyst for the degradation of an endocrine disruptor under UV and visible light irradiations. *J. Environ. Chem. Eng.* **2018**, *6*, 3757−3769.

(22) G, M.; Sivasamy, A.; GA, S. J.; Kavithaa, S. Preparation, characterization and enhanced photocatalytic activities of zinc oxide nano rods/silicon carbide composite under UV and visible light irradiations. *J. Mol. Catal. A: Chem.* **2016**, *411*, 167−178.

(23) Lee, K. M.; Lai, C. W.; Ngai, K. S.; Juan, J. C. Recent developments of zinc oxide based photocatalyst in water treatment technology: A review. *Water Res.* **2016**, *88*, 428−448.

(24) Reddy, T. N.; Manna, J.; Rana, R. K. Polyamine-mediated interfacial assembly of rGO-ZnO nanostructures: A bio-inspired approach and enhanced photocatalytic properties. *ACS Appl. Mater. Interfaces* **2015**, *7*, 19684.

(25) Etacheri, V.; Roshan, R.; Kumar, V. Mg-doped ZnO nanoparticles for efficient sunlight-driven photocatalysis. *ACS Appl. Mater. Interfaces* **2012**, *4*, 2717−2725.

(26) Mahdavi, R.; Talesh, S. S. Sol-gel synthesis, structural and enhanced photocatalytic performance of Al doped ZnO nanoparticles. *Adv. Powder Technol.* **2017**, *28*, 1418−1425.

(27) Muktaridha, O.; Adlim, M.; Suhendrayatna, S.; Ismail, I. Progress of 3d metal-doped zinc oxide nanoparticles and the photocatalytic properties. *Arabian J. Chem.* **2021**, *14*, No. 103175.

(28) Qin, H.; Li, W.; Xia, Y.; He, T. Photocatalytic activity of heterostructures based on ZnO and N-doped ZnO. *ACS Appl. Mater. Interfaces* **2011**, *3*, 3152−3156.

(29) Yu, W.; Zhang, J.; Peng, T. New insight into the enhanced photocatalytic activity of N-, C-and S-doped ZnO photocatalysts. *Appl. Catal., B* **2016**, *181*, 220−227.

(30) Pascariu, P.; Cojocaru, C.; Olaru, N.; Samoila, P.; Airinei, A.; Ignat, M.; Sacarescu, L.; Timpu, D. Novel rare earth (RE-La, Er, Sm) metal doped ZnO photocatalysts for degradation of congo-red dye: Synthesis, characterization and kinetic studies. *J. Environ. Manage.* **2019**, *239*, 225−234.

(31) Ali, A. M.; Ismail, A. A.; Najmy, R.; Al-Hajry, A. Preparation and characterization of ZnO−SiO2 thin films as highly efficient photocatalyst. *J. Photochem. Photobiol., A* **2014**, *275*, 37−46.

(32) Zhu, L. P.; Liao, G. H.; Huang, W. Y.; Ma, L. L.; Yang, Y.; Yu, Y.; Fu, S. Y. Preparation, characterization and photocatalytic properties of ZnO-coated multi-walled carbon nanotubes. *Mater. Sci. Eng. B* **2009**, *163*, 194−198.

(33) Kang, W.; Jimeng, X.; Xitao, W. The effects of ZnO morphology on photocatalytic efficiency of ZnO/RGO nanocomposites. *Appl. Surf. Sci.* **2016**, *360*, 270−275.

(34) Yadav, S.; Mittal, A.; Sharma, S.; Kumari, K.; Chauhan, N. S.; Kumar, N. Low temperature synthesized ZnO/Al₂O₃ nanocomposites for photocatalytic and antibacterial applications. *Semicond. Sci. Technol.* **2020**, *35*, No. 055008.

(35) Chen, Y. L.; Zhang, C. E.; Deng, C.; Fei, P.; Zhong, M.; Su, B. T. Preparation of ZnO/GO composite material with highly photocatalytic performance via an improved two-step method. *Chin. Chem. Lett.* **2013**, *24*, 518−520.

(36) Valiveti, V. S. K.; Singh, F.; Ojha, S.; Kanjilal, D. Influence of thermal annealing and ion irradiation on zinc silicate phases in nanocomposite ZnO−SiOₓ thin films. *Appl. Surf. Sci.* **2014**, *317*, 1075−1079.

(37) Rivera-Enríquez, C.; Fernández-Osorio, A.; Chávez-Fernández, J. Luminescence properties of α-and β-Zn2SiO4: Mn nanoparticles prepared by a co-precipitation method. *J. Alloys Compd.* **2016**, *688*, 775−782.

(38) Wahab, S. A. A.; Matori, K. A.; Zaid, M. H.; Awang Kechik, M. M.; Hj Ab Aziz, S.; Talib, R. A.; Azman, A. Z.; Khaidir, R. E.; Khiri, M. Z.; Effendy, N. A study on optical properties of zinc silicate glass-ceramics as a host for green phosphor. *Appl. Sci.* **2020**, *10*, 4938.

(39) Vashisth, A.; Khatri, S.; Hahn, S. H.; Zhang, W.; Van Duin, A. C.; Naraghi, M. Mechanical size effects of amorphous polymer-derived ceramics at the nanoscale: experiments and ReaxFF simulations. *Nanoscale* **2019**, *11*, 7447−7456.

(40) Veres, M.; Koós, M.; Tóth, S.; Füle, M.; Pócsik, I.; Tóth, A.; Mohai, M.; Bertóti, I. Characterisation of aC: H and oxygen-containing Si: C: H films by Raman spectroscopy and XPS. *Diamond Relat. Mater.* **2005**, *14*, 1051−1056.

(41) Sun, L.; Han, C.; Wu, N.; Wang, B.; Wang, Y. High temperature gas sensing performances of silicon carbide nanosheets with an n−p conductivity transition. *RSC Adv.* **2018**, *8*, 13697−13707.

(42) Askari, S.; Haq, A. U.; Macias-Montero, M.; Levchenko, I.; Yu, F.; Zhou, W.; Ostrikov, K. K.; Maguire, P.; Svrcek, V.; Mariotti, D. Ultra-small photoluminescent silicon-carbide nanocrystals by atmospheric-pressure plasmas. *Nanoscale* **2016**, *8*, 17141−17149.

(43) Singh, P.; Simanjuntak, F. M.; Wu, Y. C.; Kumar, A.; Zan, H. W.; Tseng, T. Y. Sensing performance of gas sensors fabricated from controllably grown ZnO-based nanorods on seed layers. *J. Mater. Sci.* **2020**, *55*, 8850−8860.

(44) Kushwaha, A.; Aslam, M. Hydrogen-incorporated ZnO nanowire films: stable and high electrical conductivity. *J. Phys. D: Appl. Phys.* **2013**, *46*, No. 485104.

(45) Parhi, P.; Manivannan, V. Novel microwave-initiated synthesis of Zn₂SiO₄ and MCrO₄ (M = Ca, Sr, Ba, Pb). *J. Alloys Compd.* **2009**, *469*, 558−564.

(46) Pandey, B.; Weathers, D. L. Temperature-dependent formation of ZnO and Zn₂SiO₄ nanoparticles by ion implantation and thermal annealing. *Nucl. Instrum. Methods Phys. Res., Sect. B* **2014**, *332*, 359−363.

(47) Alexander, M. R.; Short, R. D.; Jones, F. R.; Stollenwerk, M.; Zabold, J.; Michaeli, W. An X-ray photoelectron spectroscopic investigation into the chemical structure of deposits formed from hexamethyldisiloxane/oxygen plasmas. *J. Mater. Sci.* **1996**, *31*, 1879−1885.

(48) Palacios-Huerta, L.; Cabañas-Tay, S. A.; Cardona-Castro, M. A.; Aceves-Mijares, M.; Domínguez-Horna, C.; Morales-Sánchez, A. Structural and optical properties of silicon rich oxide films in graded-stoichiometric multilayers for optoelectronic devices. *Appl. Phys. Lett.* **2016**, *109*, No. 031906.

(49) Ma, J. W.; Lee, W. J.; Bae, J. M.; Jeong, K. S.; Oh, S. H.; Kim, J. H.; Kim, S. H.; Seo, J. H.; Ahn, J. P.; Kim, H.; Cho, M. H. Carrier mobility enhancement of tensile strained Si and SiGe nanowires via surface defect engineering. *Nano Lett.* **2015**, *15*, 7204−7210.

(50) Johansson, L. I.; Owman, F.; Mårtensson, P. High-resolution core-level study of 6H-SiC (0001). *Phys. Rev. B* **1996**, *53*, 13793.

(51) Dake, L. S.; Baer, D. R.; Zachara, J. M. Auger parameter measurements of zinc compounds relevant to zinc transport in the environment. *Surf. Interface Anal.* **1989**, *14*, 71−75.

(52) Yamashita, Y.; Miyahara, R.; Sakamoto, K. *Emulsion and Emulsification Technology. Cosmetic Science and Technology: Theoretical Principles and Applications*; Elsevier Inc., 2017; pp 489−506 9780128020548.

(53) Yamashita, S.; Kikkawa, J.; Yanagisawa, K.; Nagai, T.; Ishizuka, K.; Kimoto, K. Atomic number dependence of Z contrast in scanning transmission electron microscopy. *Sci. Rep.* **2018**, *8*, No. 12325.

(54) Kanjilal, A.; Gemming, S.; Rebohle, L.; Muecklich, A.; Gemming, T.; Voelskow, M.; Skorupa, W.; Helm, M. Microstructure analysis at the interface of Er decorated Ge nanocrystals in SiO2. *Phys. Rev. B* **2011**, *83*, No. 113302.

(55) Praseptiangga, D.; Zahara, H. L.; Widjanarko, P. I.; Joni, I. M.; Panatarani, C.*Preparation and FTIR Spectroscopic Studies of SiO2-ZnO Nanoparticles Suspension for the Development of Carrageenan-based Bio-nanocomposite Film*, AIP Conference Proceedings; 2020100005 DOI: 10.1063/5.0003434.

(56) Azman, A. Z.; Matori, K. A.; Ab Aziz, S. H.; Zaid, M. H.; Wahab, S. A.; Khaidir, R. E. Comprehensive study on structural and optical properties of Tm2O3 doped zinc silicate based glass−ceramics. *J. Mater. Sci.: Mater. Electron.* **2018**, *29*, 19861−19866.

(57) Ali, A. M.; Ismail, A. A.; Bouzid, H.; Harraz, F. A. Sol−gel synthesis of ZnO−SiO2 thin films: impact of ZnO contents on its photonic efficiency. *J. Sol−Gel Sci. Technol.* **2014**, *71*, 224−233.

(58) Ramakrishna, P. V.; Murthy, D. B.; Sastry, D. L.; Samatha, K. Synthesis, structural and luminescence properties of Mn doped ZnO/Zn2SiO4 composite microphosphor. *Spectrochim. Acta, Part A* **2014**, *129*, 274−279.

(59) Salh, R. Defect related luminescence in silicon dioxide network: a review. *Cryst. Silicon: Prop. Uses* **2011**, 135−172.

(60) Medina-Dzul, K.; Carrera-Figueiras, C.; Pérez-Padilla, Y.; Vilchis-Nestor, R. A.; López-Téllez, G.; Sánchez, M.; Muñoz-Rodríguez, D. SiO2/polyvinylimidazole hybrid polymer as a sorbent for extraction by matrix solid-phase dispersion (MSPD): synthesis, characterization, and evaluation. *J. Polym. Res.* **2015**, *22*, 1−9.

(61) Luna-López, J. A.; Carrillo-López, J.; Aceves-Mijares, M.; Morales-Sánchez, Y. A.; Falcony, C. FTIR and photoluminescence of annealed silicon rich oxide films. *Superficies Vacio* **2009**, *22*, 11−14.

(62) Nazarov, A. N.; Vovk, Y. N.; Lysenko, V. S.; Turchanikov, V. I.; Scryshevskii, V. A.; Ashok, S. Carrier transport in amorphous SiC/crystalline silicon heterojunctions. *J. Appl. Phys.* **2001**, *89*, 4422−4428.

(63) Kanjilal, A.; Rebohle, L.; Voelskow, M.; Skorupa, W.; Helm, M. Influence of annealing on the Er luminescence in Si-rich SiO2 layers co-implanted with Er ions. *J. Appl. Phys.* **2008**, *104*, No. 103522.

(64) Tachiki, K.; Kaneko, M.; Kobayashi, T.; Kimoto, T. Formation of high-quality SiC (0001)/SiO2 structures by excluding oxidation process with H2 etching before SiO2 deposition and high-temperature N2 annealing. *Appl. Phys. Express* **2020**, *13*, No. 121002.

(65) Kobayashi, T.; Okuda, T.; Tachiki, K.; Ito, K.; Matsushita, Y. I.; Kimoto, T. Design and formation of SiC (0001)/SiO2 interfaces via Si deposition followed by low-temperature oxidation and high-temperature nitridation. *Appl. Phys. Express* **2020**, *13*, No. 091003.

(66) Roy, J.; Chandra, S.; Das, S.; Maitra, S. Oxidation behaviour of silicon carbide-a review. *Rev. Adv. Mater. Sci.* **2014**, *38*, 29−39.

(67) Jannat, A.; Lee, W.; Akhtar, M. S.; Li, Z. Y.; Yang, O. B. *New and Effective Anti Reflection Coating of SiC-SiO2 Nanocomposite for p-type Silicon Solar Cell*, IEEE 42nd Photovoltaic Specialist Conference (PVSC); 2015 DOI: 10.1109/PVSC.2015.7356325.

(68) Narushima, T.; Goto, T.; Hirai, T. High-temperature passive oxidation of chemically vapor deposited silicon carbide. *J. Amer. Ceram. Soc.* **1989**, *72*, 1386−1390.

(69) Abed, J. *Characterization and Modification of Solar Energy Water Splitting Material for Storable Fuel Generation*; Khalifa University, 2017 DOI: 10.13140/RG.2.2.27772.33924.

(70) Highfield, J. Advances and recent trends in heterogeneous photo (electro)-catalysis for solar fuels and chemicals. *Molecules* **2015**, *20*, 6739−6793.

(71) Li, Z.; Wanjala, B.; Cernigliaro, G.; Nawrocki, D.; Gu, Z. Synthesis of Zn2SiO4@ ZnO core-shell nanoparticles and the effect of shell thickness on band-gap transition. *Mater. Chem. Phys.* **2020**, *240*, No. 122144.

(72) Zhang, T.; ki Oyama, T.; Horikoshi, S.; Hidaka, H.; Zhao, J.; Serpone, N. Photocatalyzed N-demethylation and degradation of methylene blue in titania dispersions exposed to concentrated sunlight. *Solar Energy Mater. Solar Cells* **2002**, *73*, 287−303.

(73) Guo, J.; Song, K.; Wu, B.; Zhu, X.; Zhang, B.; Shi, Y. Atomically thin SiC nanoparticles obtained via ultrasonic treatment to realize enhanced catalytic activity for the oxygen reduction reaction in both alkaline and acidic media. *RSC Adv.* **2017**, *7*, 22875−22881.

(74) Lv, J.; Gong, W.; Huang, K.; Zhu, J.; Meng, F.; Song, X.; Sun, Z. Effect of annealing temperature on photocatalytic activity of ZnO thin films prepared by sol−gel method. *Superlattices Microstruct.* **2011**, *50*, 98−106.

(75) Hu, J.; Zhong, Z.; Zhang, F.; Xing, W.; Jin, W.; Xu, N. High-efficiency, synergistic ZnO-coated SiC photocatalytic filter with antibacterial properties. *Ind. Eng. Chem. Res.* **2016**, *55*, 6661−6670.

(76) Phan, D. T.; Chung, G. S. Characteristics of ZnO films deposited on poly 3C-SiC buffer layer by Sol-Gel method. *Trans. Electr. Electron. Mater.* **2011**, *12*, 102−105.

(77) Ferhati, H.; Djeffal, F.; Bendjerad, A.; Saidi, A.; Benhaya, A. Post-annealing effects on RF sputtered all-amorphous ZnO/SiC heterostructure for solar-blind highly-detective and ultralow dark-noise UV photodetector. *J. Non-Cryst. Solids* **2021**, *574*, No. 121168.

(78) Calcagno, L.; Musumeci, P.; Roccaforte, F.; Bongiorno, C.; Foti, G. Crystallisation mechanism of amorphous silicon carbide. *Appl. Surf. Sci.* **2001**, *184*, 123−127.